Bonding and Magnetism in Nanosized Graphene Molecules: Singlet States of Zigzag Edged Hexangulenes C6m2H6m(m=2,3, ...,10)

doi: 10.1063/1.3264885

Bonding and magnetism in nanosized graphene molecules: Singlet states of zigzag edged hexangulenes $C_{6m^2}H_{6m}(m=2,3,\ldots,10)$

Michael R. Philpott[a] and Yoshiyuki Kawazoe
Institute for Materials Research, Tohoku University, Aoba-ku, Sendai 980-8577, Japan

(Received 11 June 2009; accepted 26 October 2009; published online 4 December 2009)

A novel molecular phenomenon is predicted on the basis of trends identified in an *ab initio* density functional theory study of the electronic and geometric structure of the hexagonal shaped zigzag edged graphene hydrocarbon molecules $C_{6m^2}H_{6m}(m=2,\ldots,10)$. Electrons in the interior organize to form a graphene core that grows with edge size m. Electrons in the highest occupied molecular orbital levels, localized primarily on the perimeter carbons, polarize the interior atoms with a intensity that decays rapidly with distance from the perimeter. Three distinctive bond length patterns emerge: (i) a central graphene core that grows with size m; (ii) shape-similar transverse and radial bond length patterns on interior rows close to the edges; and (iii) quinoidal bonds radiating from each apex that link adjacent edges. Concomitant with these changes are: (i) a monotonic decrease in atomic charge from center to perimeter and (ii) relegation of spin in diradical states to the outer atomic rows of the bipartite lattice. © *2009 American Institute of Physics*. [doi:10.1063/1.3264885]

I. INTRODUCTION

All nanoscale objects have surfaces that contain a significant fraction of the total number of atoms. A dichotomy arises, because the chemical bonding requirements of the surface and interior zones are not the same and surface reconstruction ensues. In an unsupported two dimensional (2D) object there is no screening of long range interactions sourced on the perimeter or on the interior. Consequently as neither is completely screened from the other the structure of the interior and the encompassing perimeter are the result of a mutual equilibrium. This is a difference compared with a three dimensional (3D) system. In polycyclic aromatic hydrocarbon (PAH) molecules the pi-systems lie outside the molecular plane and provide extended polarizable conjugative pathways that are not subject to nuclear screening in the same way as the plane centered sigma bond framework. Large compact PAH molecules, containing hundreds of sp^2 hybridized carbon atoms terminated at the perimeter by hydrogen atoms, provide the systems, where in 2D aspects of the dichotomy perimeter versus interior can be explored theoretically and experimentally.[1–3]

In large PAH molecules we expect a central region that approximates the geometry and chemical properties of infinite graphene. The environment of the bonds at the perimeter is quite different to the interior. Half of the perimeter carbons are attached to H atoms and have no outwardly directed pi-bonds. The core of graphene adds to the topological restrictions in effect at the perimeter. On a long zigzag perimeter the pi-electron highest occupied molecular orbital (HOMO)-lowest unoccupied molecular orbital (LUMO) gap can shrink to zero. Then a Peierls (Jahn–Teller) effect can change the geometry and open an energy gap in new electronic state. Theoretical studies of periodic graphene ribbons have shown that states localized on the edge can affect properties such as conductivity and magnetism.[4–14] Chemical modification of edges of epitaxial grown graphene layers has been pursued experimentally and studied theoretically.[15,16] Edge states also affect the geometry of nanoribbons[17] however this turns out not to be as large an effect in simple zigzag ribbons as in molecules. In ribbons the core geometry controls positions in the periodic direction. Displacements in the perpendicular direction then become much more limited than in molecules.

Considering large PAHs and not infinite systems, there was pioneering work on large hexagonal shaped molecules by Stein and Brown.[18] They use Hückel and extended Hückel theory and structure resonance theory and were able to examine systems with several thousand atoms within the approximations inherent to Hückel theory. This was an important contribution. In the more recent period, several papers have appeared that describe the band structure and possible magnetism of graphene strips at various levels of approximation. Two papers considered various aspects of hexagonal shaped systems[19,20] in a general way but did not report on the geometry or electronic structure at the level of detail provided here. However one important conclusion was that the hexangulene with $m=8$ had an antiferromagnetic ordering of spin[19] in the ground state. The calculations described here predict the $m=9$ system as the first such candidate. Studies predicting magnetism in small to medium sized graphene molecules have also appeared.[21] In this paper we continue the density functional theory (DFT) study of the electronic structure and geometry of this new sub category of PAHs, referred to here as graphene molecules.[17,22–24] Some other molecules have been included for comparison.

Figure 1 shows in cartoon of all the molecules discussed in this report. We refer to the molecules studied here as hexangulenes and where no confusion is possible abbreviate them as hex m-zzg or m-zzg. The states examined include a diradical singlet $S=0$ ground state ($m \geq 9$) and the lowest

[a]Author to whom correspondence should be addressed. Electronic mail: philpott@imr.edu.

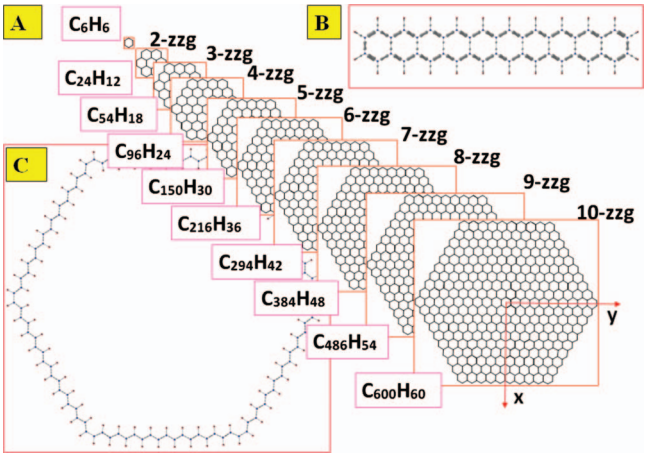

FIG. 1. A schematic diagram showing: (a) the D_{6h} symmetric zigzag hexangulene molecules $C_{6m^2}H_{6m}(m=2,3,\ldots,10)$; (b) decacene $C_{42}H_{24}$ the $m=10$ member of the series of D_{2h} symmetric linear acenes $C_{4m+2}H_{2m+4}(m=2,3,\ldots)$; and (c) 114-annulene $C_{114}H_{114}$ the $m=10$ member of the series of D_{6h} annulenes $C_{6(2m-1)}H_{6(2m-1)}(m=2,3,\ldots)$.

spin paired singlet S=0 state. Detailed information concerning the lowest diradical triplet S=1 state will be reported elsewhere. The electronic structure of the perimeter of (hex) 10-zzg is compared with the edge structure in the D_{2h} symmetric linear acene decacene $C_{42}H_{24}$ the $m=10$ member of the series $C_{4m+2}H_{2m+4}(m=2,3,\ldots)$. Decacene has two zigzag edges coupled by "cross-tie" CC bonds of similar lengths to the hex 10-zzg graphene. The linear acenes are of interest because calculations indicate the appearance of a diradical single state in the range $m=7-8$.[22,25–27] The hexagonal shaped annulenes $C_{6(2m-1)}H_{6(2m-1)}$, where $m=2,3,\ldots$ (Ref. 28) provide useful edge only models for the entire perimeter of the hexangulenes. We compare the hypothetical $m=10$ annulene molecule with hex 10-zzg. In all the calculations reported here we have used the same computational methodology in order that the evolution of trends can be followed with confidence into the region of small HOMO-LUMO energy gaps. Four trends are followed as the molecular size (measured by an increase in the zigzag edge parameter m or the diameter parameter $2m-1$) is increased: (i) development of a graphenelike core with uniform carbon-carbon bonding; (ii) evolution of a perimeter on which the apex bonds become the shortest in the molecule and their pinning of a series of alternating bonds tending to uniform bond length at midedge; (iii) an oscillation in CC bond lengths plotted versus distance from the molecular center and the appearance of quinoidal bond patterns at the apexes; and (iv) the trend in the two outer most bond sets, one (transverse) connecting atoms on the perimeter and the second (radial) connecting the last two rows, as they become the source of a polarizing interaction that impresses their row pattern on each interior row of bonds.

This paper is organized as follows: next we provide a sparse account of the computational method, then a description of the maximum isometric surface charge (MISC) followed by the labeling scheme for bonds. This is followed by Sec. V summarizing the trends in the DFT energy calculations. Section VI describes the trends in geometry and in separate subsections provides some details for each of the ($m\leq 9$) zigzag systems. This is followed by Sec. VII for the largest system ($m=10$), including a description of the properties of the spin paired singlet and the diradical singlet ground state. Section VIII provides a summary and discussion. Computed DFT energies for the hexangulenes and the annulenes are listed in two tables in Sec. V.

II. COMPUTATIONAL METHOD

The calculations in this report used *ab initio* plane wave based DFT methodology[29–32] with Blöchl's projector augmented wave (PAW) frozen core potentials[33,34] and the spin polarized generalized gradient approximation with the exchange-correlation energy functional (PW91) parameterized by Perdew and co-worker.[35] Valence electrons were assigned: C(4) and H(1). All the calculations were performed using periodic boundaries with a simulation cell chosen so that all atoms in adjacent cells were at least 1.5 nm apart. In a preliminary series of calculations an orthorhombic unit cell was used that mimicked the $x:y$ aspect ratio of the hexagonal shape of each molecule. In a second series of calculations a tetragonal box was used with the smallest box having dimensions $2.5\times2.5\times1.5$ nm^3 and the largest one with $6.5\times6.5\times1.5$ nm^3 side lengths. Brillouin zone integrations were done at the gamma point. The plane wave energy cutoff was 400 eV. Integration grids were generally set ten to twenty percent higher than the values recommended for the routines. We also ran calculations for the ground state of the $m=8$ member $C_{384}H_{48}$ with an energy cutoff equal to 500 eV to verify that the CC bond lengths oscillated with distance from the molecular center. The geometry optimization was performed using D_{2h} constrained dynamics. Nevertheless the geometry of the ground states were found only slightly distorted off D_{6h} symmetry for the entire series of molecules. In all cases, increasing the density of points on the integration grids and tightening the energy convergence tolerance for ionic movements to 0.0005 eV resulted in residual in-plane forces on all atoms with magnitudes less than 0.000 34 eV/Å. The residual forces acting on atoms in the graphene interior zone were noticeably smaller than those near the perimeter. In the present study we have calculated: geometry, total energy, isometric surfaces of total charge density and spin; atom centered electric charge and spin. The use of a single determinant as done here to represent the spin properties of open shell systems has been widely investigated in recent years.[36,37] It is not without significant problems in cases where charge transfer occurs. The strategy of this project was use the same methodology to follow a series of molecules into the large size regime in order to identify and document evolution in structure and provide interpretations that rely on trends observed along the series. This requires that we provide some detailed documentation in the form of compact figures for each molecule. Some useful CC bond values were calculated using the same methodology with larger energy cutoff (500 eV) and larger simulation cell: benzene CC=139.6(5) pm (box $2\times2\times2$ nm^3); graphene CC=142.5 pm.

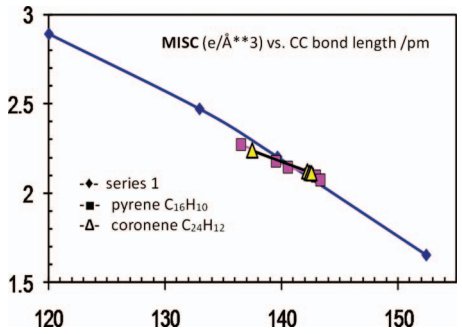

FIG. 2. Plots of the MISC density ($e/Å^3$) vs CC bond length (pm). Series 1: acetylene C_2H_2, ethylene C_2H_4, benzene C_6H_6, and ethane C_2H_6 (-◆-, range 120–153 p.m.). PAHs: pyrene $C_{16}H_{10}$ (-■-) and coronene $C_{24}H_{18}$ (-▲-).

III. MAXIMUM ISOMETRIC SURFACE CHARGE DENSITY

For any bond between atoms we define the MISC density as the threshold charge density beyond which no charge is visible on the stick connecting the atoms. In an earlier paper (see Fig. 9 in the paper[23]) we noted that there was a linear dependence between MISC and the measured bond distance for CC bonds in several compact aromatic hydrocarbons. We have extended this plot to include molecules with single, double and triple CC bonds. Figure 2 shows MISC electron density ($e/Å^3$) versus CC bond length (pm) for the extended set of hydrocarbons. The nature of chemical bonds between atoms has been admirably set out in the work on atoms-in-molecules by Bader.[38] For this paper it is sufficient to note that changes in the MISC density across the molecule can be monitored using the CC bond length as a surrogate measure.

IV. NOTATION AND LABELS

We start by defining some the abbreviations: hex for hexangulene, ace for linear acene and ann for annulene. We use the word perimeter only to describe the outer most set of carbon atoms. Recall that the zigzag parameter m is the number of C_6 rings on the edge of the hexangulene molecule and the diameter is $(2m-1)$ C_6 rings wide.

Figure 3 shows the scheme for labeling the CC bonds of the zigzag hexangulenes using the (+,+)-quadrant of the 10-zzg molecule. Every carbon atom belongs to a hexagonal row of atoms. These rows form a nested set labeled by an integer $n=1,2,3,\ldots,10$. All the CC bonds occur in one of two types of hexagonal shaped row around the molecule. Transverse bonds run in zigzag fashion around the hexagonal shaped rows of carbon atoms. We label the zigzag bond rows by an integer $n=1,2,3,\ldots,10$. Radial bonds join carbon atoms belonging to adjacent zigzag rows. We label the rows of radial bonds by a half odd integer starting at $n=1.5,2.5,3.5,\ldots,9.5$. For example, bonds in the row 3.5 are radial bonds that join atoms in (zigzag) rows 3 and 4. It is also mnemonically useful to introduce an alphabetical scheme for labeling CC bonds. We label all bond rows alphabetically a,b,c,… (without regard for type) starting from the central C_6 ring. These two labeling schemes provide a compact and useful notation for labeling plots of CC bond

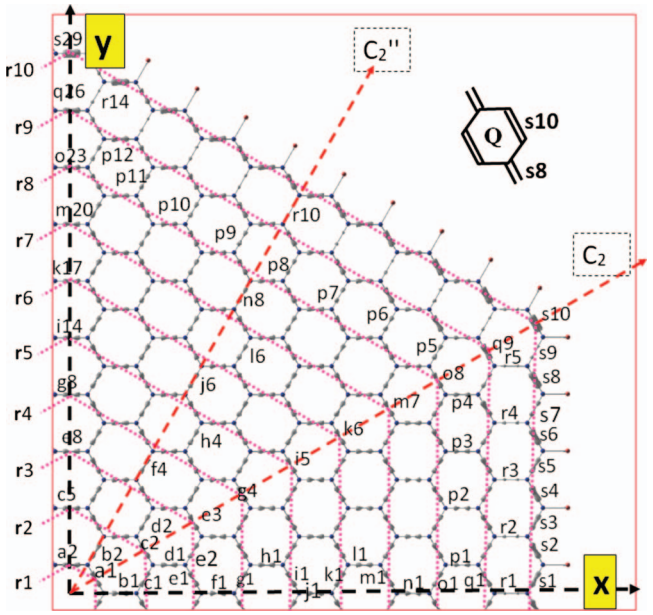

FIG. 3. CC bond labeling scheme superimposed on the optimized geometry of hex 10-zzg $C_{600}H_{60}$ with an isometric surface of valence charge for density ($\rho_{iso}=2.034$ $e/Å^3$) in the (+,+)-quadrant of the molecule. The inset structure **Q** denotes a quinoidal chemical bond structure. See Sec. IV for a detailed explanation of the notation.

length along rows and for comparing bond lengths in different rows. Bonds along a given row are numbered sequentially 1,2,3,… in a counterclockwise fashion starting from the x-axis. In Fig. 3 the lines (⋯⋯) trace out the nested hexagonal rows of carbon atoms. These rows are labeled **r**1, **r**2, …, **r**10 on the left hand side next to the y-axis. In some Figures and in the text we occasionally use a hybrid notation such as **r**3.5(f3) which specifies the CC bond 3 in radial row **r**3.5. The additional alphabetic label "f" in this case though superfluous is useful in helping one identify and verify the location of a bonds in a large molecule.

There are other features in Fig. 3 that require comment. The inset structure **Q** denotes a quinoidal chemical bond structure to be described later. The dashed straight lines (− − −) show four of six C_2 rotation axes of a D_{6h} symmetric molecule. Two such axes coincide with the x- and y-axes. Also shown in the Fig. 3 is the optimized geometry of hex 10-zzg $C_{600}H_{60}$ for the spin paired singlet state and an isometric surface of total valence charge at density ($\rho_{iso}=2.034$ $e/Å^3$). Note that on the perimeter (**r**10) and penultimate (**r**9) rows the isometric surfaces of the CC bonds appear with three basic shapes. Cylinders for the short apex bonds (s10 and s29), dumbbells (see bonds s2 and s3) and as two small centroids (see radial bonds joining the perimeter to the next inner row).[39]

V. TRENDS IN ENERGY

The Tables I and II list the DFT energies for the hexangulenes and annulenes including the singlet-triplet state differences and HOMO-LUMO gaps displayed in the Figs. 4–6 of this section. Some of the data for the hexangulenes and linear acenes has been published in a preliminary report.[22] In the tables the column under ΔE refers to the difference in the

TABLE I. DFT-PAW energies (eV) of hex *m*-zzg molecules $C_{6m^2}H_{6m}(m=1,2,\ldots,10)$.

System State/symmetry	−Energy (cell)	ΔE	BG_0 or BG_{00} $BG_1;BG_2$
C_6H_6/1-zzg	20×20×20 Å^3		
S0/D_{6h}	76.23 eV	0.00	5.10
S1-av/D_{2h}	72.26 eV	3.97	1.2;1.0
$C_{24}H_{12}$/2-zzg	25×25×15 Å^3		
S0/D_{6h}	262.99 eV	0.00	2.87
S1-av/D_{2h}	260.51 eV	2.47	0.44;0.42
$C_{54}H_{18}$/3-zzg	30×30×15 Å^3		
S0/D_{6h}	560.31 eV	0.00	1.904
S1-av/D_{2h}	558.62 eV	1.69	0.24;0.23
$C_{96}H_{24}$/4-zzg	35×35×15 Å^3		
S0/D_{6h}	968.28 eV	0.00	1.35
S1a-av/D_{2h}	967.04 eV	1.24	0.15;0.15
$C_{150}H_{30}$/5-zzg	40×40×15 Å^3		
S0/D_{6h}	1487.01 eV	0.00	0.99
S1/D_{2h}	1486.14 eV	0.87	0.11;0.11
$C_{216}H_{36}$/6-zzg	45×45×15 Å^3		
S0/D_{6h}	2116.51 eV	0.00	0.73
S1-av/D_{2h}	2115.89 eV	0.62	0.04;0.10
$C_{294}H_{42}$/7-zzg	50×50×15 Å^3		
S0/D_{6h}	2856.87 eV	0.00	0.54
S1-av/D_{2h}	2856.44 eV	0.43	0.10;0.10
$C_{384}H_{48}$/8-zzg	55×55×15 Å^3		
S0/D_{6h}	3708.08 eV	0.00	0.39
S1/D_{2h}	3707.75 eV	0.33	0.00;0.00
$C_{486}H_{48}$/9-zzg	60×60×15 Å^3		
S00/D_{6h}	4670.23 eV	0.00	0.34
S0/D_{6h}	4670.22 eV	0.02	0.28
S1/D_{2h}	4670.09 eV	0.14	0.15;0.17
$C_{600}H_{60}$/10-zzg	65×65×15 Å^3		
S00/D_{6h}	5743.32 eV	0.00	0.34
S0/D_{6h}	5743.20 eV	0.12	0.20
S1/D_{2h}	5743.23 eV	0.09	0.19;0.18

TABLE II. DFT-PAW energies (eV) of annulene *m*-zzg molecules $C_{6(2m-1)}H_{6(2m-1)}(m=2,3,\ldots,10)$.

System State/symmetry	−Energy (cell)	ΔE	BG_0 or BG_{00} $BG_1;BG_2$
$C_{18}H_{18}$/2-zzg	25×25×15 Å^3		
S0/D_{6h}	226.32 eV	0.00	1.86
S1/D_{2h}	224.88 eV	1.44	0.53;0.50
$C_{30}H_{30}$/3-zzg	30×30×15 Å^3		
S0/D_{6h}	377.82 eV	0.00	1.08
$C_{42}H_{42}$/4-zzg	35×35×15 Å^3		
S0/D_{6h}	529.23 eV	0.00	0.86
S1/D_{2h}	528.58 eV	0.649	0.28;0.27
$C_{54}H_{54}$/5-zzg	40×40×15 Å^3		
S0/D_{6h}	680.63 eV	0.00	0.67
$C_{66}H_{66}$/6-zzg	45×45×15 Å^3		
S0/D_{6h}	832.02 eV	0.00	0.55
S1/D_{2h}	831.61 eV	0.41	0.20;0.20
$C_{90}H_{90}$/8-zzg	55×55×15 Å^3		
S0/D_{6h}	1134.82 eV	0.00	0.41
S1/D_{2h}	1134.53 eV	0.29	0.17;0.17
$C_{102}H_{102}$/9-zzg	60×60×15 Å^3		
S0/D_{6h}	1286.23 eV	0.00	0.36
S1/D_{2h}	1285.98 eV	0.26	0.15;0.15
$C_{114}H_{114}$/10-zzg	65×65×15 Å^3		
S0/D_{6h}	1437.63 eV	0.00	0.32
S1/D_{2h}	1437.41 eV	0.23	0.15;0.15

energy of the specified state relative to the ground state. The HOMO-LUMO gap is defined as BG_0 for spin paired singlet and BG_{00} for singlet diradical state. The HOMO-LUMO gap BG_1 and BG_2 refer to HOMO-LUMO gaps in the spin 1 (up) and spin 2 (down) energy manifold. In the Figs. 4–6, which plot data for hexangulenes, annulenes and linear acenes, we use the following common set of symbols: (-♦-) for BG_0 the HOMO-LUMO gap of spin paired singlet state; (-■-) for $\Delta E_{10}=ES_1-ES_0$ the energy difference of the lowest triplet and the spin paired singlet state; (-▲-) for BG_{00} the HOMO-LUMO gap of singlet diradical ground state (GS); (-●-) for $\Delta E_{000}=ES_0-ES_{00}$ the energy difference of spin paired singlet and diradical singlet GS; (-★-) for $\Delta E_{100}=ES_1-ES_{00}$ the energy difference of triplet state and singlet diradical ground state (GS).

Figure 4 shows a plot of the HOMO-LUMO levels and energy differences for the zigzag hexangulenes $C_{6m^2}H_{6m}(m=6,7,\ldots 10)$. The data show BG_0 and ΔE_{10} plotted out to $m=10$. The diradical state is lowest energy state for $m=9$ and 10. The three short curves plot data for $m=9$, 10 relative to the diradical ground state energy. For hex 10-zzg the energy $\Delta E_{10}(10)=-0.03$ eV. This marks a triplet state "crash" analogous to the result known from DFT calculations of the linear acenes.[22,25–27] In Fig. 6 we plot the acene data over the same range to show the same dependence. In both cases the DFT model predicts the appearance of a diradical state with antiferromagnetically arranged spins. These states are disjoint diradicals meaning in the that the spin 1 and spin 2 densities are on separate sublattices.

Figure 5 shows the HOMO-LUMO gap BG_0 data and lowest triplet state energy difference $\Delta E=ES_1-ES_0$ plotted for the annulenes $C_{6(2m-1)}H_{6(2m-1)}(m=2,\ldots,10)$. The variation in energy does not show the initial dramatic monotonic drop of either the hexangulenes or linear acenes (see Fig. 4 and Fig. 6). The smaller drop in energy difference with parameter *m* reflects the simpler nature of the "box" states of a cyclic single strand pi-system. The geometry of the annulenes shows almost no variation in bond length on zigzag

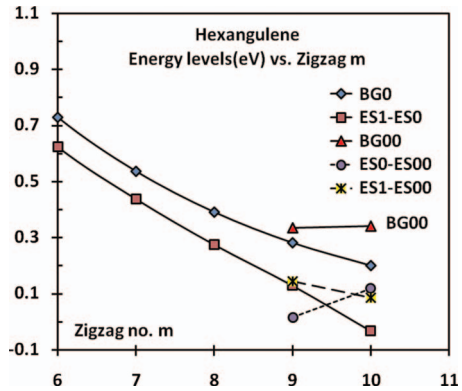

FIG. 4. Plots of the Kohn–Sham HOMO-LUMO energy gap and state energy differences (eV) vs the zigzag parameter *m* for the hexangulenes $C_{6m^2}H_{6m}(m=6,\ldots 10)$.

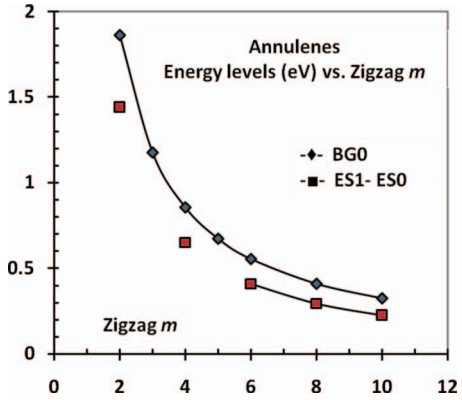

FIG. 5. Plots of the Kohn–Sham HOMO-LUMO energy gap and state energy differences (eV) vs the zigzag parameter m for the annulenes $C_{6(2m-1)}H_{6(2m-1)}(m=2,\ldots,10)$.

sections. This is a trend that only starts to develop in the hexangulenes and the acenes when the edges get long $(m \geq 10)$.

Figure 6 shows the HOMO-LUMO and energy data for the linear acene molecules $C_{4m+2}H_{2m+4}(m=5,3,\ldots,10)$ with the same labels and notation used in Figs. 4 and 5. This system has been studied many times. In the linear acenes the DFT HOMO-LUMO level gap BG_0 becomes small and the computed DFT triplet state "crashes" past the singlet energy. In DFT calculations of the acenes a new ground appears at $m=7$ or 8 (this calculation) with antiferromagnetically ordered spins. In such a singlet diradical state[40] the spin up and spin down density occurs on the separate sub-lattices of the bipartite lattice of the carbon atoms.[41] In the linear acenes the precise nature of this state has been controversial. Studies have commented on the properties of a singlet diradical configuration and the extent of spin contamination of the ground state.[25–27]

For the purposes of this paper we note that pattern of Kohn–Sham levels and state energies in Fig. 6 is basically the same as shown in Fig. 4. This is an intriguing new association. It suggests that the mechanism underlying the appearance of an antiferromagnetically ordered spin state in the

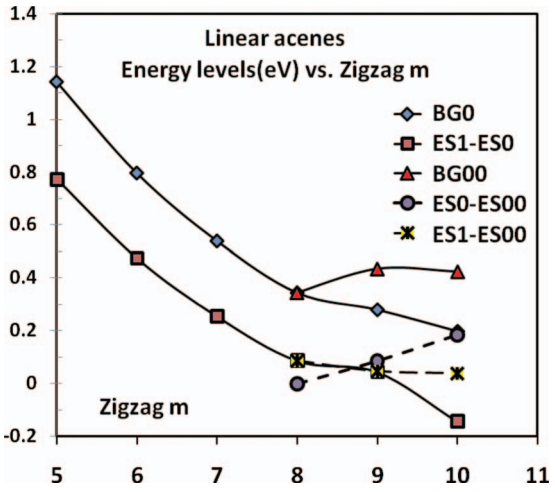

FIG. 6. Plots of the Kohn–Sham HOMO-LUMO energy gap and state energy differences (eV) vs the zigzag parameter m for the linear acenes $C_{4m+2}H_{2m+4}(m=5,\ldots,10)$.

two molecules has common elements. It also raises new questions concerning polyradical and multiradical states of graphene molecules. True poly radicals have been synthesized with the magnetic centers isolated and not part of either a bipartite lattice or pi-systems joined by a conjugated set.[42] Whether the spin of the electronic ground state of a conjugated molecule could depend on the length of the molecule is an open question. The transition from finite graphene molecules to nanoribbons infinite appears to be a vexing problem.

VI. TRENDS IN GEOMETRY

The introduction listed four trends in geometry that appear and evolve as the molecular size increases. This section contains a brief description of all the hexangulenes $m=2,\ldots,9$. We present plots of the CC bond length versus row index (integer for transverse and half-odd integer for radial bonds). Smooth curves are drawn through the data points to guide the eyes. Portions of the valence charge density isometric surfaces are also given labeled so that key bond patterns can be identified. Theoretical interpretation of how the valence charge density around the edge of the molecule influences the interior is postponed to Sec. VIII. The chief trend in the geometry is the growth of the graphene core. The core has a quite uniform geometry that aids its stabilization by electronic resonance. The core places significant topological constraints on the zigzag edges. The geometry of perimeter can be thought of as the result of two opposing trends. At each apex there is a short CC bond (similar to an ethylene double bond) with long bonds on either side. This geometric feature is present in the smallest member coronene $C_{24}H_{12}$. As the sides of the hexangulene get longer the bond lengths of the middle edge carbon atoms tend toward a uniform value. This midedge feature emerges slowly with increase zigzag number m. The series can be broken into three groups. The group with $m=2,3,4$ show the origins of the features present in the largest systems. The second $m=5,6,7,8$ exhibits expanding features with a recognizable graphene core. The third set with $m=9,10$ show the trends established in the smaller molecules and a new transition to a magnetic ground state.

A. Hex 2-zzg coronene $C_{24}H_{12}$

In Fig. 7 panel A shows the converged geometry of the singlet ground state $(D_{6h}, S=0)$ and a superimposed isometric surface of total charge $(\rho_{iso}=2.017\ e/Å^3)$. The colored background represents the total valence charge density in a linear color scale on the xy-plane containing the nuclei (color online). The sigma bond net work is shown by the orange-red colored density. The calculated DFT bond lengths (pm) are: transverse a1=142.6; radial b1=142.4; transverse c1=c3=142.2; c2=c5=137.4. The bonds c2=c5 and c3=c1 not shown in the figure are related by symmetry. The calculated bond lengths are in overall agreement with the 1966 crystal structure data[43] though strict comparison is limited because the reported rotational disorder in the crystal. This molecule has the smallest carbon net work in the current series and there is no evidence of the oscillation in bond

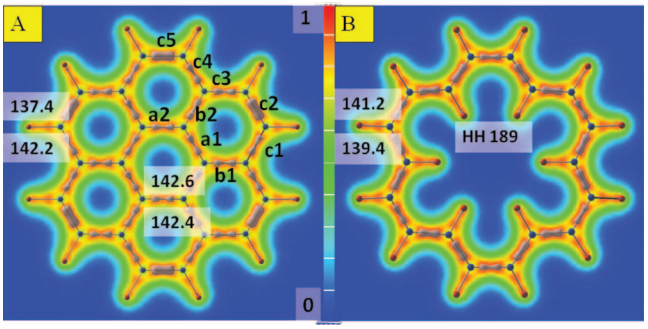

FIG. 7. DFT results for the molecules coronene $C_{24}H_{12}$ and [18]-annulene $C_{18}H_{18}$. The total charge density on the *xy*-plane through the nuclei is shown on a linear color scale. Panel A shows the converged geometry of coronone with a superimposed isometric surface of total charge for the singlet ground state (D_{6h}, S=0; ρ_{iso}=2.017 e/Å^3). Panel B shows the isometric surface at a similar density for 18-annulene.

length versus row number found in the larger members. Figure 7 panel B shows a plot of the converged ground state geometry of 18-annulene (ann 2-zzg, $C_{18}H_{18}$) with an isometric surface plot for the ground state charge density. The calculation was for a D_{6h} geometry. The features in Fig. 7 panels A and B can be compared because the maximum charge densities of both molecules were very nearly the same. Note that the structure of the perimeters of the two molecules are quite different. The 18-annulene has a "long" apex bond whereas in coronene and the larger hexangulenes the apex bond is short. The "longer" apex bond (CC=141.2 pm) is a distinguishing feature of the annulenes. At DFT-PAW level of computation the annulene edge bonds CC=139.4 pm are very close to the computed benzene length (benzene CC=139.6 pm). We postpone further comparisons of geometry to Sec. VII, where a comparison of edge bonds in hex-, ann- and ace-10-zzg is described in conjunction with Fig. 15.

B. Hex 3-zzg circumcoronene $C_{54}H_{18}$

All the results of the DFT calculation for circumcoronene $C_{54}H_{18}$ are summarized in separate panels in Fig. 8. Panel A shows an isometric surface of the total charge at a density a little smaller than in the case of the 2-zzg molecule. The geometry is summarized by the data plotted in panels B, C and D of Fig. 8. In panels A and B the individual bonds are identified by the alphabetic notation. Symmetry equivalent bonds have the same label. In contrast to coronene (2-zzg), Fig. 8 panel B shows this molecule a hint of the interior bond length oscillation that develops as the molecules increase in size. The longer perimeter of 3-zzg compared with 2-zzg shows a vestige of the alternation in the perimeter bonds (see row index **r**3, Fig. 8 panel D) that dominates the perimeter of the large systems.

C. Hex 4-zzg $C_{96}H_{24}$

Figure 9 displays a summary of the DFT results for hex 4-zzg in the singlet ground state. Panel A shows an isometric surface of the total valence charge density at a sufficiently high density (ρ_{iso}=2.095 e/Å^3) that there is no charge enclosed on the last row of radial bonds. Examples are the

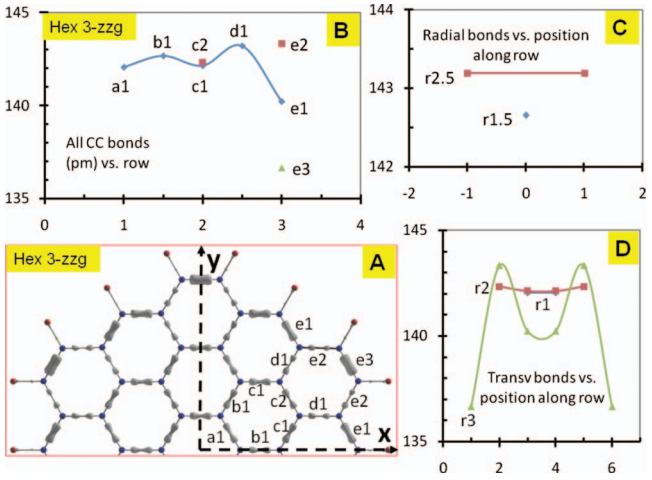

FIG. 8. Summary DFT results for hex 3-zzg circumcoronene $C_{54}H_{18}$. Panel A shows an isometric surface of the total charge density. Panel B shows all CC bond lengths (pm) vs row number for all bond rows. Panel C shows the variation in length (pm) of radial bonds along rows **r**1.5 and **r**2.5. Panel D shows the variation in length (pm) of the transverse bonds along rows r1 (center, hidden under **r**2), **r**2, and **r**3 (perimeter). See Sec. IV for an explanation of the notation.

radial bonds labeled f1 and f2 in panels A and B. Panel B shows all the CC bonds plotted versus row index number. In panel B the radial bonds f1 and f2, which are among the longest in the molecule, are shown on row **r**3.5. Panel C shows the variation in length of the radial bonds along the three rows with indexes **r**1.5, **r**2.5, and **r**3.5. Although there are few symmetry distinct bonds, the radial bonds have constant length on their row. They show a decrease in length from row to row in the direction of the center of the molecule. Panel D shows the variation in length of transverse bonds along the four hexagonal (center **r**1, **r**2, **r**3, and perimeter **r**4). Datum point on row **r**1 is masked by data belonging to rows **r**2 and **r**3. Note that there is a prominent alternation in bond length along the perimeter row **r**4, and no

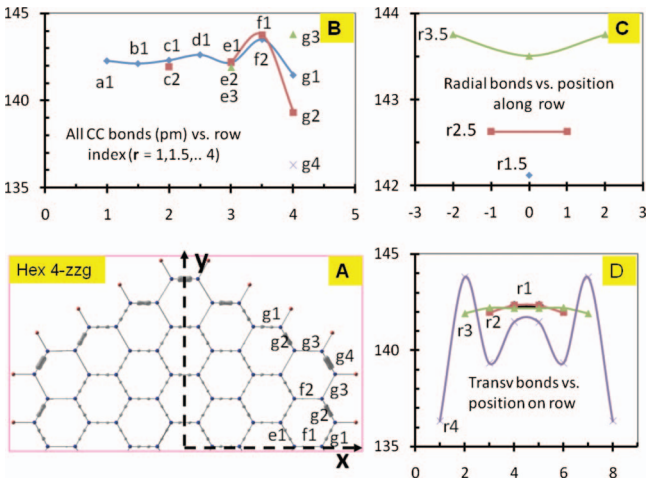

FIG. 9. Summary DFT results for the molecule hex 4-zzg $C_{96}H_{24}$. Panel A shows an isometric surface of the total valence charge density at a high value. Panel B shows all the CC bonds lengths (pm) plotted vs row index number for all bond rows. Panel C shows variation in length (pm) of the radial bonds along three rows. Panel D shows the variation in length (pm) of the transverse bonds along four hexagonal rows. See Sec. IV for an explanation of the notation.

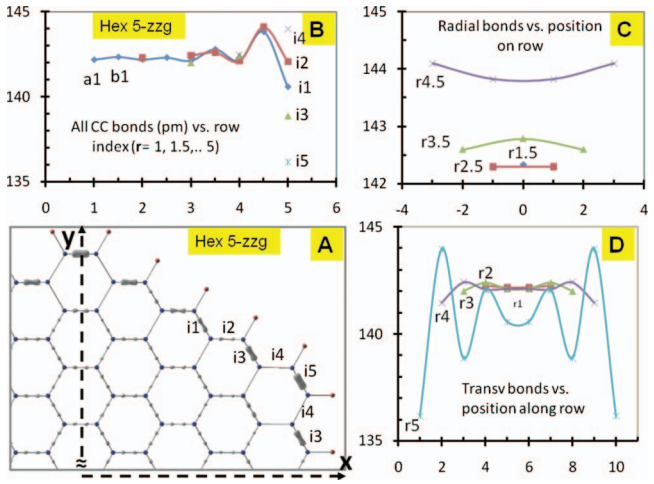

FIG. 10. Summary DFT results for the molecule hex 5-zzg $C_{150}H_{30}$. Panel A shows a portion of a high density value isometric surface of the total valence charge density. Panel B shows all the CC bonds lengths (pm) plotted vs row number. Panel C shows the radial bond length (pm) variation along rows $\mathbf{r}1.5,\ldots,\mathbf{r}4.5$. Panel D shows the transverse bond length (pm) variation along rows $\mathbf{r}1$ (center),…, $\mathbf{r}5$ (perimeter). See Sec. IV for an explanation of the notation.

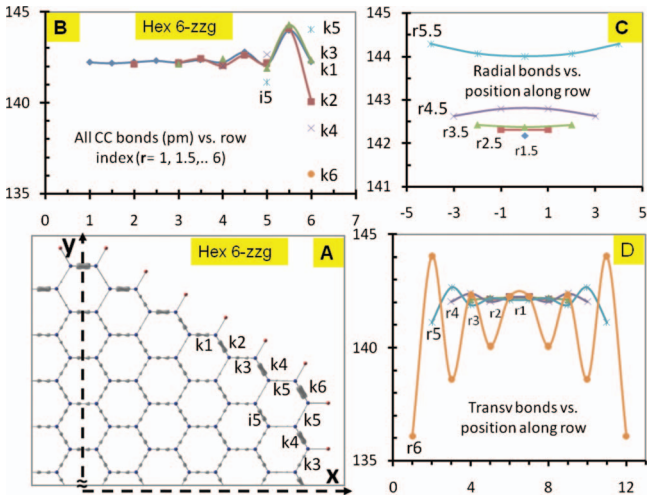

FIG. 11. Summary DFT results for the molecule hex 6-zzg $C_{216}H_{36}$. Panel A shows an isometric surface of the total valence charge density at high value (ρ_{iso}=2.058 e/Å^3). Panel B shows all the CC bond lengths (pm) plotted vs row index number. Panel C shows the radial bond length (pm) variation along rows $\mathbf{r}1.5,\ldots,\mathbf{r}5.5$. Panel D shows the transverse bond length (pm) variation along rows and the appearance of a self-similar pattern in the variation of transverse bond lengths in going from row to row starting from the perimeter. See Sec. IV for an explanation of the notation.

evidence of alternation on the interior rows $\mathbf{r}3$ and $\mathbf{r}2$. Taken together the bond length variations suggest this molecule is the first in the series to contain a graphene core, which is roughly the size of coronene.

D. Hex 5-zzg $C_{150}H_{30}$

The hex 5-zzg DFT results are summarized in Fig. 10 panels A, B, C, and D. The isometric surface of total charge density in panel A (ρ_{iso}=2.083 e/Å^3) corresponds to the absence of a charge isometric surface on radial bonds connecting the perimeter to the rest of the molecule. Panel B shows all the CC bonds plotted versus row number. The labels (i1,…,i5) on the perimeter row $\mathbf{r}5$ shows the large range in perimeter bond lengths. Panel C shows variation in length of the radial bonds along bond rows with indexes $\mathbf{r}1.5,\ldots,\mathbf{r}4.5$. There is little length variation along a given row. However, starting with a big initial jump, there is a monotonic decrease from row to row converging on the graphene bond length at the center. Panel D shows the variation in length of the transverse bonds along rows $\mathbf{r}1$ (center),…, $\mathbf{r}5$ (perimeter). The row r1 data is masked by higher numbered rows. The perimeter row in particular shows the range of bond variations found in the large m systems. Finally we note that the region with little or no CC bond length oscillation in panel B shows that the graphene core has expanded to the radius of row $\mathbf{r}3$. The increase in the size of the core with m is an established trend. Likewise the migration of the strongly oscillating bond region with the perimeter away from center is an established trend.

E. Hex 6-zzg $C_{216}H_{36}$

The results of the DFT calculations for hex 6-zzg are summarized in panels A, B, C, and D of Fig. 11. The isometric surface density in panel A is ρ_{iso}=2.058 e/Å^3. As before this value is high enough to distinguish the outer radial bond set ($\mathbf{r}5.5$) by the absence of charge. The symmetry distinct perimeter bonds k1 (midedge), k2,…,k6 (apex) are labeled in panel A and panel B. Panel C shows that the radial bonds belonging to the same row have almost the same length. Panel D shows a strong length alternation starting at the apex bond k6 decreasing toward the middle of the edge. The row $\mathbf{r}1$ data is masked by higher numbered rows. There is a new feature apparent in panel D. Notice that the variation in transverse bonds lengths along the perimeter is repeated in a self-similar pattern on the interior rows. This has been be verified by expanding the length scale for transverse bond lengths on rows $\mathbf{r}5$ and $\mathbf{r}4$. We postpone discussion of this effect to Sec. VIII. A second feature weakly visible in panel A is the presence of a quinoidal bond pattern (see Fig. 3 inset **Q**) involving the bonds (k5, k6, and i5) of the apex C_6-ring and the bonds k4 on either side.

F. Hex 7-zzg $C_{294}H_{42}$

Figure 12 with panels A, B, C, and D summarizes the DFT results for valence charge density and bond length data for molecule $C_{294}H_{42}$. In panel A the isometric charge density (ρ_{iso}=2.053 e/Å^3) was set just below the threshold for the appearance charge in the radial bonds of row $\mathbf{r}6.5$ which joins the perimeter to the rest of the molecule. The symmetry distinct set of perimeter bonds [(midedge) m1, m2,…, (apex) m7] with labels in panel A belong to row $\mathbf{r}7$. They fall in a wide length range as indicated by the data points labeled in panel B. The new trend, that appeared first in hex 6-zzg, is the quinoidal pattern of CC bonds in each apex. It involves the bonds (k6, m6, and m7) of the apex C_6-ring and the bonds m5 on either side. This quinoidal structure is part of a pattern extending out on either side of the apex and is visible in all the larger systems. The apex pattern has C_{2v} symmetry not the full D_{2h} symmetry of the quinoidal molecule 1,4

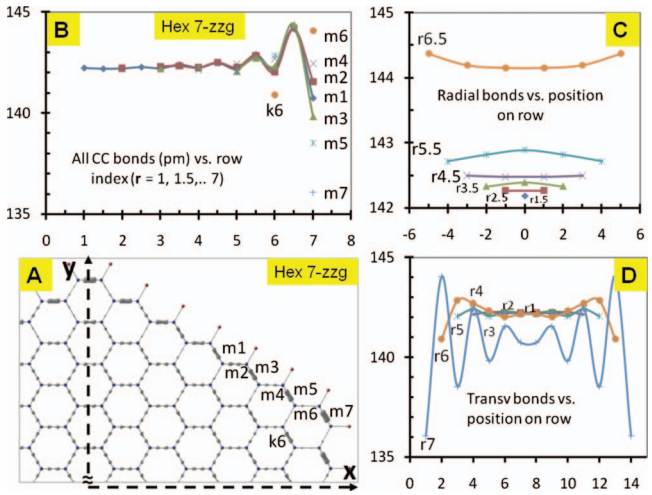

FIG. 12. Summary DFT results for the molecule hex7-zzg $C_{294}H_{42}$. Panel A shows an isometric surface of the total valence charge density at a high value. The charge density shows an extended quinoidal (see Fig. 3 panel Q) bond pattern in the apex that links adjacent edges. Panel C shows the radial bond length (pm) variation along rows $\mathbf{r}1.5,\ldots,\mathbf{r}6.5$. Panel D shows the transverse bond length (pm) variation along rows $\mathbf{r}1$ (center), …, $\mathbf{r}7$ (perimeter). See Sec. IV for an explanation of the notation.

dimethylene benzene $CH_2{=}C_4H_4{=}CH_2$. Consequently the "double" bonds on opposite sides of the C_6-ring have different charge densities.

The existence of the quinoidal pattern explains why there is an oscillation of CC bonds depicted in all the panels B (starting with Figs. 8–14). It is a direct result of the development of a linked pattern of quinoidal structures connecting adjacent edges. This is an important result linking edge topology to interior structure.

G. Hex 8-zzg $C_{384}H_{48}$

This molecule is the largest in the present series with a spin paired singlet (S=0) ground state. From Table I the calculated HOMO-LUMO gap BG_0=0.39 eV and the triplet-singlet state energy difference is ΔE=0.33 eV. Attempts to find a lower energy state using spin polarized initial states were not successful. In the interesting paper by Fernandez-Rossier *et al.*[19] a diradical singlet ground state was found for this system. The appearance of the new spin polarized ground state clearly involves a delicate balance of competing interactions and the way they are represented in the computational methodology. The situation encountered here is similar to the DFT study of the linear acenes series where a singlet diradical ground state can appear at either m=7 or 8 depending on the computational method being used.[22,25–27]

In Fig. 13 the panels A, B, C, and D summarize the results for hex 8-zzg $C_{384}H_{48}$. Panel A shows part of the (+,+)-quadrant with two apexes separated by their edge. The isometric surface of charge density has ρ_{iso}=2.094 e/Å^3. there is almost no charge enclosed on the bonds in last radial row $\mathbf{r}7.5$. The panels A and B show symmetrically distinct perimeter bonds using alphabetical labels. The quinoidal bond pattern at the apex involves bonds o6, o7, o8, and m7. Panel C shows radial bond length variation along rows $\mathbf{r}1.5,\ldots,\mathbf{r}7.5$. Panel D shows the transverse bond length variation along rows $\mathbf{r}1$ (center),…, $\mathbf{r}8$ (perimeter). The row $\mathbf{r}1$ data is masked by higher numbered rows. Panel D shows The shape-similar effect is well developed in the outer rows of transverse bonds. In Fig. 13 panels B, C, and D collectively show the convergence of CC bonds in the interior. The

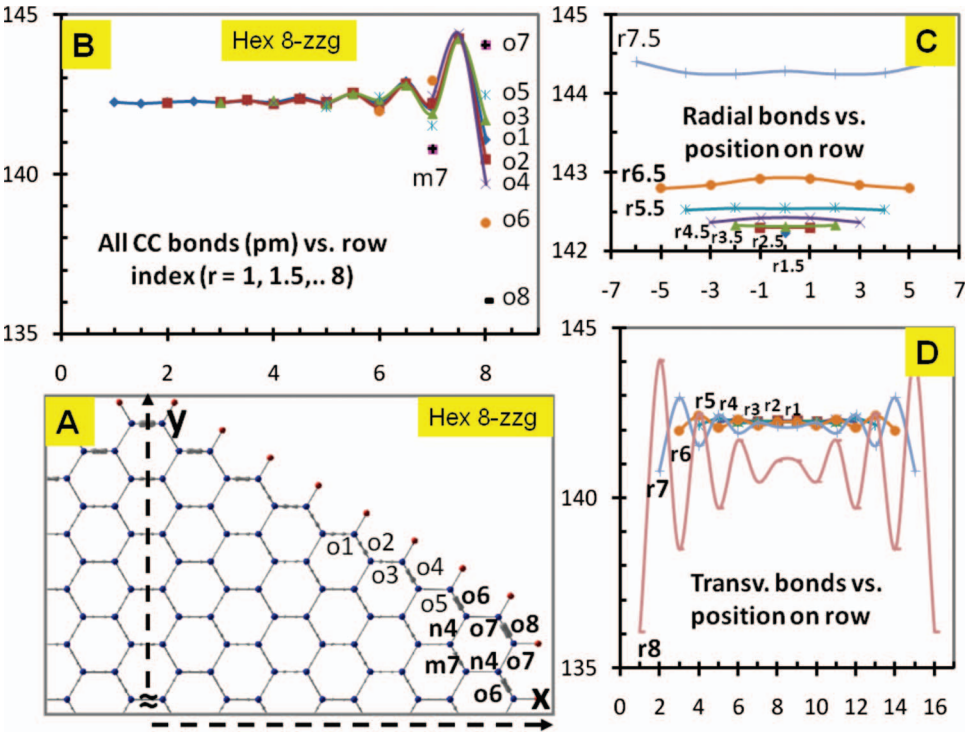

FIG. 13. Summary of the DFT results for the molecule hex 8-zzg $C_{384}H_{48}$. Panel A shows an isometric surface of the total valence charge density. Panel B shows all the CC bond lengths (pm) plotted vs row number. Panel C shows the radial bond length (pm) variation for rows r1.5,…,r7.5. Panel D shows the transverse bond length (pm) variation along rows r1 (center),…,r8 (perimeter). Note that the shape-similar effect is well developed in the outer rows. See Sec. IV for an explanation of the notation.

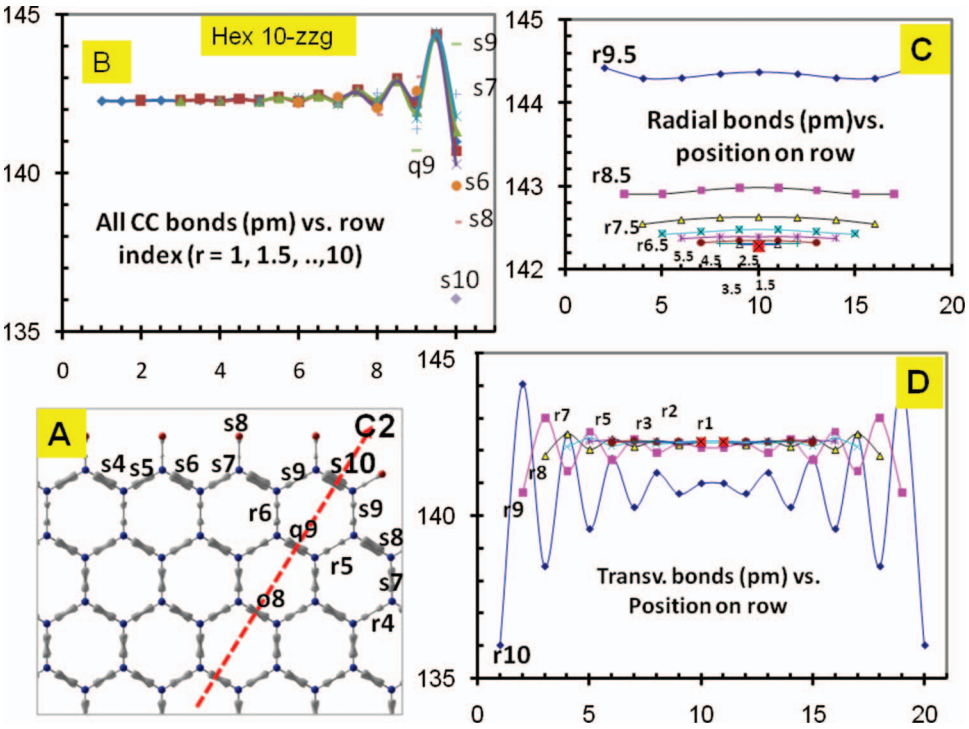

FIG. 14. Summary DFT results for the molecule hex 10-zzg $C_{600}H_{60}$ in the spin paired singlet state. Panel A shows an isometric surface of the total valence charge density. Panel B shows all the CC bonds lengths (pm) plotted vs row index number. Panel C shows radial bond length (pm) variation along rows. Panel D shows the transverse bond length (pm) variation along rows. See Sec. IV for an explanation of the notation.

central zone has uniform CC bond length out to transverse row index **r**5. At the center of the molecule the bond length CC ~142.2 pm. The longest bonds in the molecule separate the two outer most hexagonal rows of atoms CC=144.4 pm. At the apex there are long bonds (CC≈144 pm) flanking the shortest bonds (CC≈136 pm). The bond alternation pattern along the perimeter starting at the apex is: CC=136(apex)-144-138-142-140-142-140-141-141-140-142-140-142-138-144-136 (apex)pm. This pattern shows that bond alternation is greatly diminished at the center of the edge. An indication of increased electron delocalization in the middle of the edge.

H. Hex 9-zzg $C_{486}H_{54}$

This molecule was the first in the series to have a singlet diradical ground state. Altogether three low lying configurations were located: two singlets and one triplet. The ground-triplet state energy difference was 0.12 eV (see Table I). The optimized geometries of the three states were very similar. We defer a discussion of the properties of this diradical ground state to Sec. VII B. There we describe and discuss instead the results for hex 10-zzg which are similar. In a separate report[17] we have described the geometry of the singlet spin paired configuration. We have analyzed the variation of the bond lengths along the rows and demonstrated that the bond length patterns are self-similar when account is taken for the difference in the number of bonds on the row.

VII. HEX 10-ZZG $C_{600}H_{60}$

Table I lists the energies of the three lowest electronic states using the DFT model. We describe here only the singlet states starting with the spin paired singlet state.

A. Singlet spin paired state

In Fig. 14 we show a summary set of results in four panels. In the calculation the geometry optimization was constrained to D_{2h}. Nevertheless when the residual forces were reduced to the level described in the computational section (Sec. II), the geometry was very close to D_{6h} and this was taken to be the symmetry of the spin paired singlet state. Subsequent analysis of total and partial Kohn–Sham level charge densities did not suggest a different symmetry.

Figure 3 panel A showed the isometric charge density at $\rho_{iso}=2.034$ e/Å^3 in which the radial bonds of row **r**9.5 were close to threshold (note small charge centroids). See for example radial bonds with alphabetical labels r1–r5, r10, and r14 in Fig. 3. The bonds of the interior have more prominent

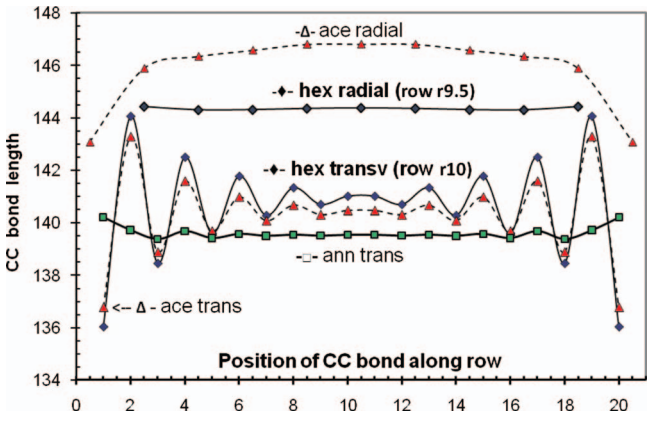

FIG. 15. Comparison of the DFT edge (transverse and radial) bond lengths (pm) for singlet spin paired state of hex 10-zzg $C_{600}H_{60}$, 10-zzg $C_{42}H_{24}$ and ann 10-zzg $C_{114}H_{114}$. Note the similarity between transverse bonds for the hexangulene and the acene.

centroids meaning they are shorter. In Fig. 14 panel A we show an isometric surface at a lower charge density (ρ_{iso} = 1.993 e/Å^3) and each radial bonds in bond row **r**9.5 have two small charge centroids. In isometric surface plots at lower charge density it becomes more difficult to differentiate between the various bonds. Note that the portion of the charge isometric surface detailed in Fig. 14 (panel A) shows a quinoidal structure located on the apex bisected by rotation axis C_2. The short bonds s8, s10, and q9 define the quinoidal pattern together with the long bonds r5 and s9. This central quinoid form is the most prominent one of a series of linked quinoidal structures stretching out on either side of the apex.

In Fig. 14 panel B the smooth curves drawn through the data points are essentially flat from center to nested carbon row **r**6 or **r**7. In this molecule the graphene zone is a dominant feature. If the tolerance for a graphene zone were set at $CC_g = 142.5 \pm 0.25$ pm then from Fig. 14 panel B we could take the zone as extending as far as transverse bond row index **r**6. Panel C shows the radial bond lengths hardly change at all along their rows (index **r**1.5 to **r**9.5). The radial bonds in row **r**9.5(CC=144.4 pm) are the longest in the molecule. The range within any row is approximately 0.2 p.m. or less. The radial bond length converges quickly, dropping to the graphene value as the bond row approaches the molecular center at row **r**1.5. Panel D shows the transverse bond length variation along rows **r**1 (center),…, **r**10 (perimeter). The row **r**1 data are masked by higher numbered rows. Panel D shows that the transverse bonds have a different behavior. In contrast to the radial bonds the transverse bonds vary strongly along their row. Also the midedge value increases as the row approaches the center of the molecule.

Figure 15 compares the perimeter of the graphene molecule hex 10-zzg with the perimeter of acene 10-zzg $C_{42}H_{24}$ and the perimeter of ann 10-zzg $C_{114}H_{114}$. We note that there is a very strong similarity between the hexangulene and the acene but not so much to the annulene. Recall that it was suggested in the introduction that the annulene could be regarded as an isolated perimeter without any topological interference from radial bonds. However as Fig. 15 shows the bonds in ann 10-zzg resemble acene 10-zzg and hex 10-zzg only at midedge where the short CC bond lengths imply there is a region of strong electronic conjugation. Returning to Fig. 14 panel D, we note the shape-similarity of CC bond length pattern from row to row. If the vertical energy scale is enlarged then we find the bond patterns are the same except for length. This description fits the radial bonds which have flat curves. The polarization of interior bonds in a pattern determined by the edge bond sets (rows **r**10 and **r**9.5) is a previously unrecognized phenomenon. We have reported some details in the brief paper.[17]

Next we examine localization of (partial) charge density in the Kohn–Sham HOMO and LUMO levels close to the Fermi level and contrast them with levels lying deeper and higher. In Fig. 16 the panels A, B, C, and D shows the partial charge density labeled for selected KS-levels of hex 10-zzg arrayed in a quadrant. The complete charge distribution can be found by reflecting a given quadrant in the *x*- and *y*-axes to generate a full hexagon. Panel A displays the charge density of the combined partial charges of HOMOs 1 and 2

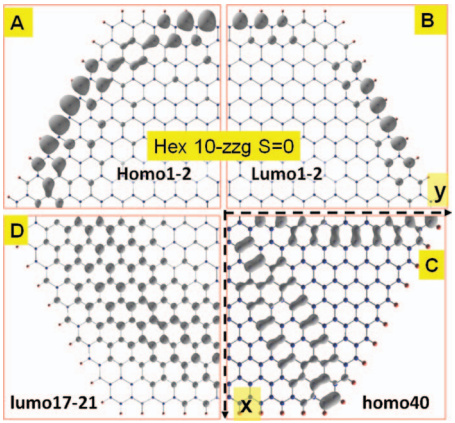

FIG. 16. DFT results for the molecule hex 10-zzg $C_{600}H_{60}$ in the spin paired state. The quadrants show isometric surfaces of partial charge for Kohn–Sham HOMOs and LUMOs: (panel A) the edge localized HOMO; (panel B) the edge localized LUMO; (panel C) a delocalized interior HOMO; and (panel D) the combined charge of several delocalized interior LUMOs. A complete charge distribution is obtained by reflecting the quadrant in the *x*- and *y*-axes. See the text for more details.

(degenerate pair, four electrons). We see that the HOMO 1–2 are an edge localized pair, the only charge density of significance is on the perimeter row **r**10. The symmetry of the (partial) charge distribution is D_{6h}. These are members of the set of mostly edge localized levels and they carry the polarization charge responsible for the bond length variations discussed in this paper. The edge localization is a new feature characteristic of large zigzag graphene molecules. Levels with edge localization will occur for all large graphene molecules. Panel B shows the combined partial charge for the degenerate pair LUMO 1–2. This is an edge localized LUMO level. The LUMO partial charge is localized almost exclusively on the perimeter carbon atoms.

In principle there is no symmetry that separates edge and interior levels. So between extreme edge localized levels and extreme interior levels there are some with both characteristics. In Fig. 16 panel C shows the partial charge for HOMO 40 a deep level with mostly interior localized charge. This level has a six bladed propeller appearance. Within each blade the charge is quite uniformly distributed from edge to center. Panel D shows the combined partial charge for four "high" LUMOs 17–21, a set of closely spaced LUMO levels located 1.04 eV above HOMO-1. The drum skin or "polomint" appearance of this level is apparent. For this level there is neither perimeter charge and nor central charge.

B. Singlet diradical state

The geometry of the diradical singlet S=0 state of 10-zzg is not very different from that of the singlet spin paired state. However to reach the diradical state it was necessary to remove all symmetry constraints and start the geometry optimization in an initial spin distribution corresponding to a diradical on a hexagonally sectored bipartite lattice. Figure 4 showed the HOMO-LUMO and state energy differences for the larger hexangulenes. The energy separation from the spin paired state is approximately $(ES_0\text{-}ES_{00}) \approx 0.12$ eV and the diradical HOMO-LUMO gap $BG_{00} \approx 0.34$ eV is larger than the spin paired manifold gap $BG_0 \approx 0.2$ eV. The geometric

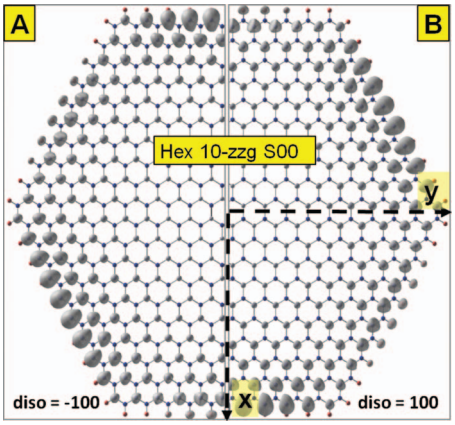

FIG. 17. DFT results for the singlet diradical state of hex 10-zzg $C_{600}H_{60}$ showing two quadrants of the total spin distribution. Note that the distribution is bipartite, disjoint and hexagonally sectored. Panels A and B show the total spin density of equal magnitude but opposite sign for isometric surfaces at a low spin density. See text for definition of spin density units.

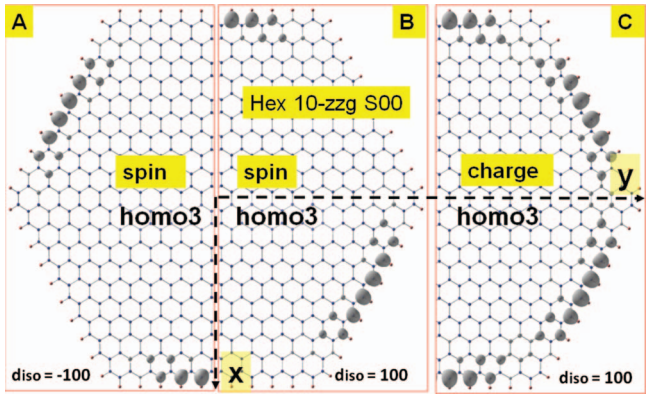

FIG. 18. Edge localized partial density of spin (panel A spin-down, panel B spin-up) and charge (panel C) for the nondegenerate HOMO-3 level of hex 10-zzg $C_{600}H_{60}$ in the singlet diradical state. Each panel represents two quadrants of the distribution. A complete distribution is obtained by reflecting in the vertical axis. The spin distribution is hexagonally sectored and disjoint, meaning atoms with spin up do not have any spin down component. The charge of the densities in panels A and B when added is equal to the charge in panel C. See text for definition of spin density units.

shifts accompanying the emergence of the magnetic ground state were small. Not surprisingly we found that there were smaller differences in geometry between the singlet diradical and the triplet state We focus here on the spin density distribution. Figure 17 shows the isometric surfaces of the total spin density on one half of the hex 10-zzg. Reflection on the *x*-axis provides the missing part of the distributions. Panels A and B show the spin density of equal magnitude but opposite sign for isometric surfaces of low spin density. The highest spin density occurs on the perimeter and the penultimate rows carbon atoms. The spin density alternates in sign going around the edges in a sequential fashion. It follows a bipartite lattice.[41] The spin density from LHS panel A to right-hand side panel B switches from one lattice to the other. The spin densities of a given sign is hexagonally sectored with the result that the total spin is zero. Spin densities are small numbers therefore it is convenient to use units ($d_{iso}=v_{cell}\times\rho_{iso}$) scaled by the simulation cell volume (see Table I). The left side shows the isometric surface for spin $d_{iso}=-100$ and the right side the spin distribution at $d_{iso}=100$. The range of spin values in scaled units is ($d_{min}=-14470, d_{max}=14470$). This is equivalent to maximum spin density of $\rho_{iso}=0.25$ spins/Å^3. The spin distribution is characteristic of a disjoint radical.[40] The highest spin density is on the perimeter and penultimate row carbon atoms.

Figure 18 shows the isometric surfaces of partial charge density of the non degenerate level HOMO-3 of the hex 10-zzg $C_{600}H_{60}$ in the diradical state. The complete charge map is obtained by refection in the vertical (*x*-axis) axis. This figure illustrates the strong localization of charge density in the highest HOMOs (and by inference lowest LUMOs) in the singlet diradical ground state. The three panels show: panel A spin "down" $d_{iso}=-100$; panel B spin "up" $d_{iso}=100$; panel C total charge ($d_{iso}=100\equiv\rho_{iso}=0.0017$ spins/Å^3). The spin density in these figures has a low value (one spin shared equally among 600 atoms$\equiv$0.0017). For calibration we mention that maximum spin density was $d_{max}=4189.2\equiv\rho_{iso}=0.072$ spins/Å^3). The total charge has sixfold symmetry about the center of the molecule.

VIII. DISCUSSION

In this section we present a brief theoretical discussion of valence polarization mechanism and follow it with a discussion of the geometry of large zigzag hexangulenes.

A. Electronic charge distribution and the mechanism of valence charge polarization

The DFT computation gave the geometry of the combined pi-manifold and sigma-manifold. It included electronegativity differences between carbon and hydrogen, which contribute to the unique carbon atom environment on the perimeter. We need however to interpret the changes in the geometry predicted by the DFT calculations. First we consider that pi-electrons are mobile and their confinement delimited by the nuclei. The confinement energy is high when lateral dimensions are small. In coronene the HOMO-LUMO gap is large $BG_0\approx 2.9$ eV. The resonance stabilization of the molecule includes contributions from the perimeter carbons. With an increase in the zigzag edge length the coulomb confinement box is larger and the band gap BG_0 decreases. The calculations show that as the graphene interior grows pi-coupling to the edges weakens because the radial CC bond lengths get longer. By analogy with the band theory of doped semiconductors, the difference in pi-bonding at the surface compared with the interior provides the interaction that creates a set of levels localized at the edge of the molecule. Edge localized levels appear at the top of the valence band or at the bottom of the conduction band. Whether they separate from the manifold depends on their strength and the dimension of the system. The mechanism is analogous to but is not identical to that described in the Koster-Slater theory of impurity levels[44] in semiconductors. In the Koster theory the physics is dominated by the diagonal matrix element and real space separation of the impurities, neither of these apply to the graphenes.

The total valence charge density is the sum of separate contributions from all the Kohn–Sham orbitals. We have ex-

amined the partial charge density of the highest(lowest) HOMOs (LUMOs) and verified that both are highly localized on the perimeter carbon atoms. In addition there is a small "spillover" to the next and next nearest neighbor nested rows of carbon. The KS-levels found at the HOMO-LUMO gap resemble the edge localized states identified in semiempirical theories of zigzag edged periodic nanoribbons.[5,6] The partial charge of highest HOMOs (and spin in the case of the diradical states) was localized on the outer edge rows. The charge distribution in the perimeter and radial CC bonds connecting to the perimeter impressed a secondary polarization on the interior bonds in a shape-similar fashion that decayed rapidly with distance from the perimeter. This is interpreted as due to charge of the occupied edge levels. The charge density summed over all occupied levels altered the bond length giving rise to the patterns measured. Though the patterns diminished greatly with distance from the perimeter, they were not screened to zero as would happen in a 3D system.

B. Structure of a large zigzag edged hexangulenes

First we summarize the geometry changes: (i) core growth with uniform CC bonding; (ii) perimeter evolving an alternating bond set with lengths becoming even toward the midedge; (iii) isolation of the perimeter through radial bond length increase; and (iv) quinoidal bond pattern linking hexagonal edges at each apex.

The CC bonds showed a shape-similar dependence from row to row. Along each row the transverse bonds showed a position dependence that mimicked the perimeter set. Likewise the radial bonds showed essentially no dependence on their position in the row following the pattern set in the outermost radial bond row (index **r**9.5). These shape dependencies resulted in the quinoidal patterns of charge density, that linking the edges joined at each apex. It also resulted in the appearance of the oscillation (radial $\geq$ transverse) when all bonds were plotted versus their row index. The electronic changes along the series from small to large m are summarized as follows: (i) monotonic decrease in atomic charge from the center to the perimeter; (ii) at $m=9$ the ground state switches from a singlet spin paired with no magnetization to a singlet disjoint diradical state with antiferromagnetic magnetization; (iii) spin when it is present ($m>8$) is relegated to the outer atomic rows; and (iv) the spins are arranged antiferromagnetically in hexagonal sectors on a bipartite lattice.

ACKNOWLEDGMENTS

All the calculations were performed on the IMR SR11000 Hitachi super computer. The authors thank the staff of the Super Computer Facility for their dedicated support. M.R.P. thanks the Japan Society for the Promotion of Science for research support. The referees are thanked for their constructive criticisms.

[1] Y. Kobayashi, K. I. Fukui, T. Enoki, and K. Kusakabe, Phys. Rev. B **73**, 125415 (2006).
[2] J. C. Meyer, C. O. Girit, M. F. Crommie, and A. Zettl, Nature (London) **454**, 319 (2008).
[3] C. O. Girit, J. C. Meyer, R. Erni, M. D. Rossell, C. Kisielowski, L. Yang, C.-H. Park, M. F. Crommie, M. L. Cohen, S. G. Louie, and A. Zettl, Science **323**, 1705 (2009).
[4] D. J. Klein, Chem. Phys. Lett. **217**, 261 (1994).
[5] M. Fujita, K. Wakabayashi, K. Nakada, and K. Kusakabe, J. Phys. Soc. Jpn. **65**, 1920 (1996).
[6] K. Nakada, M. Fujita, G. Dresselhaus, and M. S. Dresselhaus, Phys. Rev. B **54**, 17954 (1996).
[7] T. Yamamoto, T. Noguchi, and K. Watanabe, Phys. Rev. B **74**, 121409 (2006).
[8] E. Rudberg, P. Salek, and Y. Liu, Nano Lett. **7**, 2211 (2007).
[9] Y.-W. Son, M. L. Cohen, and S. G. Louie, Nature (London) **444**, 347 (2006).
[10] M. Y. Han, B. Ozyilmaz, Y. Zhang, and P. Kim, Phys. Rev. Lett. **98**, 206805 (2007).
[11] V. Barone, O. Hod, and G. E. Scuseria, Nano Lett. **6**, 2748 (2006).
[12] K. Wakabayashi and K. Harigaya, J. Phys. Soc. Jpn. **72**, 998 (2003).
[13] K. Sawada, F. Ishii, M. Saito, S. Okada, and T. Kawai, Nano Lett. **9**, 269 (2009).
[14] N. Gorjizadeh, A. A. Farajian, K. Esfarjani, and Y. Kawazoe, Phys. Rev. B **78**, 155427 (2008).
[15] D. Gunlycke, J. Li, J. W. Mintmire, and C. T. White, Appl. Phys. Lett. **91**, 112108 (2007).
[16] M. Maruyama and K. Kusakabe, J. Phys. Soc. Jpn. **73**, 656 (2004).
[17] M. R. Philpott and Y. Kawazoe, Phys. Rev. B **79**, 233303 (2009).
[18] S. E. Stein and R. L. Brown, J. Am. Chem. Soc. **109**, 3721 (1987).
[19] J. Fernandez-Rossier and J. J. Palacios, Phys. Rev. Lett. **99**, 177204 (2007).
[20] W. L. Wang, S. Meng, and E. Kaxiras, Nano Lett. **8**, 241 (2008).
[21] D.-E. Jiang, B. G. Sumpter, and S. Dai, J. Chem. Phys. **127**, 124703 (2007).
[22] M. R. Philpott, F. Cimpoesu, and Y. Kawazoe, Mater. Trans. **49**, 2448 (2008).
[23] M. R. Philpott, F. Cimpoesu, and Y. Kawazoe, Chem. Phys. **354**, 1 (2008).
[24] M. R. Philpott and Y. Kawazoe, Chem. Phys. **358**, 85 (2009).
[25] K. N. Houk, P. S. Lee, and M. Nendel, J. Org. Chem. **66**, 5517 (2001).
[26] M. Bendikov, H. M. Duong, K. Starkey, K. N. Houk, E. A. Carter, and F. Wudl, J. Am. Chem. Soc. **126**, 7416 (2004).
[27] J. Hachmann, J. J. Dorando, M. Aviles, and G. K.-L. Chan, J. Chem. Phys. **127**, 134309 (2007).
[28] F. Sondheimer, Acc. Chem. Res. **5**, 81 (1972).
[29] G. Kresse and J. Hafner, Phys. Rev. B **47**, 588 (1993).
[30] G. Kresse and J. Hafner, Phys. Rev. B **49**, 14251 (1994).
[31] G. Kresse and J. Furthmüller, Comput. Mater. Sci. **6**, 15 (1996).
[32] G. Kresse and J. Hafner, Phys. Rev. B **54**, 11169 (1996).
[33] P. E. Blöchl, Phys. Rev. B **50**, 17953 (1994).
[34] G. Kresse and D. Joubert, Phys. Rev. B **59**, 1758 (1999).
[35] J. P. Perdew and Y. Wang, Phys. Rev. B **45**, 13244 (1992).
[36] I. de P. R. Moreira, R. Costa, M. Filatov, and F. Illas, J. Chem. Theory Comput. **3**, 764 (2007).
[37] F. Illas, I. de P. R. Moreira, J. P. Bofil, and M. Filatov, Phys. Chem. Chem. Phys. **8**, 645 (2006).
[38] R. F. W. Bader, *Atoms in Molecules: A Quantum Theory* (Oxford University Press, New York, 1990).
[39] C. A. Coulson and M. W. Thomas, Acta Crystallogr., Sect. B: Struct. Crystallogr. Cryst. Chem. **27**, 1354 (1971).
[40] *Diradicals*, edited by W. T. Borden (Wiley, New York, 1982).
[41] E. H. Lieb, Phys. Rev. Lett. **62**, 1201 (1989).
[42] A. Rajca, J. Wongsriratanakul, and S. Rajca, Science **294**, 1503 (2001).
[43] J. K. Fawcett and J. Trotter, Proc. R. Soc. London, Ser. A **289**, 366 (1966).
[44] G. F. Koster and J. C. Slater, Phys. Rev. **95**, 1167 (1954).